ACS APPLIED MATERIALS & INTERFACES

www.acsami.org

Research Article

In Situ Studies of the Swelling by an Electrolyte in Electrochemical Doping of Ethylene Glycol-Substituted Polythiophene

Lucas Q. Flagg, Lauren E. Asselta, Nicholas D'Antona, Tommaso Nicolini, Natalie Stingelin, Jonathan W. Onorato, Christine K. Luscombe, Ruipeng Li, and Lee J. Richter*

Cite This: *ACS Appl. Mater. Interfaces* 2022, 14, 29052–29060

Read Online

ACCESS | Metrics & More | Article Recommendations | Supporting Information

ABSTRACT: Organic mixed ionic electronic conductors (OMIECs) have the potential to enable diverse new technologies, ranging from biosensors to flexible energy storage devices and neuromorphic computing platforms. However, a study of these materials in their operating state, which convolves both passive and potential-driven solvent, cation, and anion ingress, is extremely difficult, inhibiting rational material design. In this report, we present a novel approach to the in situ studies of the electrochemical switching of a prototypical OMIEC based on oligoethylene glycol (oEG) substitution of semicrystalline regioregular polythiophene via grazing-incidence X-ray scattering. By studying the crystal lattice both dry and in contact with the electrolyte while maintaining potential control, we can directly observe the evolution of the crystalline domains and their relationship to film performance in an electrochemically gated transistor. Despite the oEG side-chain enabling bulk electrolyte uptake, we find that the crystalline regions are relatively hydrophobic, exhibiting little (less than one water per thiophene) swelling of the undoped polymer, suggesting that the amorphous regions dominate the reported passive swelling behavior. With applied potential, we observe that the $\pi-\pi$ separation in the crystals contracts while the lamella spacing increases in a balanced fashion, resulting in a negligible change in the crystal volume. The potential-induced changes in the crystal structure do not clearly correlate to the electrical performance of the film as an organic electrochemical transistor, suggesting that the transistor performance is strongly influenced by the amorphous regions of the film.

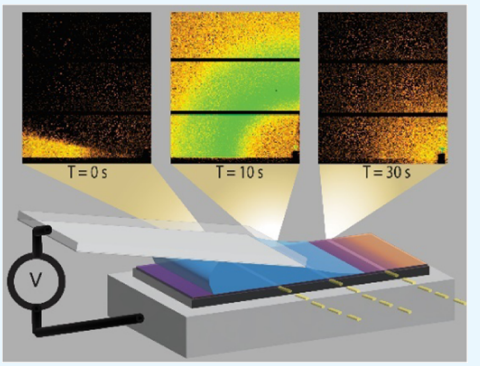

KEYWORDS: *organic electrochemical transistors, organic electronics, organic semiconductors, organic mixed ionic electronic conductors, in situ diffraction, grazing-incidence wide-angle scattering*

INTRODUCTION

Organic mixed ionic electronic conductors (OMIECs) have the potential to enable diverse new technologies,[1−3] ranging from biosensors[4,5] to flexible energy storage devices[6,7] and neuromorphic computing platforms.[8,9] As an electronic element, OMIECs enable organic electrochemical transistors (OECTs), where, unlike in the conventional field-gated thin-film transistor (TFT), mobile carriers are induced in the bulk of the semiconductor and compensated by the ingress of electrolyte counterions. The vast majority of OMIECs explored to date are based on polymers with semiconducting backbones where selectively engineered side chains confer the desired functionality. The backbone structure is often that of an established organic semiconductor (OSC) such as regioregular polythiophene,[10] polydiketopyrrolopyrrole,[11] and polynapthalene-diimide.[12] For the alkyl side-chain versions of these polymers, the structure−function relationships are well understood in terms of the hierarchy of order. In general, intrachain hopping is most facile and rapid charge transport is associated with a minimal torsional disorder in the conjugated backbone,[13] which can be achieved by either synthesis (rigid motifs) or crystal packing.[14] For semicrystalline materials, intergrain transport is facilitated by amorphous cilia or tie chains.[15,16] The two keys of local order and connectivity give rise to clear correlations between transport and both crystalline order and molecular mass.

In contrast to TFTs, where the capacitance of the gate dielectric and dielectric breakdown typically limit carrier densities to $\approx 10^{19}$ cm^{-3}, OECTs can often achieve carrier densities approaching 10^{21} cm^{-3}.[2] Therefore, their behavior is often correlated to that of chemically doped films, which have been studied extensively, particularly in the context of thermoelectrics.[17] One of the most extensively studied OSCs, both field-gated (TFT) and doped, is regioregular poly-3-hexylthiophene (P3HT). When operated as a TFT, P3HT devices typically exhibit a mobility, μ, of $10^{-3}-10^{-2}$ cm^2/(V s). It is notable that, when highly doped, P3HT exhibits a mobility

Received: April 8, 2022
Accepted: May 30, 2022
Published: June 13, 2022

https://doi.org/10.1021/acsami.2c06169
ACS Appl. Mater. Interfaces 2022, 14, 29052−29060

of $>10^{-1}$ $cm^2/(V\ s)$.[18] This increase in mobility with doping has been attributed to trap filling in variable range hoping transport[18] or a structural transition in the crystalline domains, driven by counterion insertion.[19] Similar high mobilities (relative to TFT controls) are reported for OECTs.

The operational state of an OECT differs from a dry TFT due to direct contact with an electrolyte, which enables solvent (swelling),[20] anion,[21] and cation[22] ingress. These species can stress/modify the structure in both the crystalline and amorphous regions of the film. A number of recent reports highlight the importance of both passive and active (bias-driven) swelling to both the device performance and cycling stability.[23−25] Most of these studies have been limited to probing the bulk film swelling via a quartz-crystal microbalance (QCM) due to difficulty in the interrogation of the crystal lattice in contact with the electrolyte. Many OECT studies show the effect of ex situ doping via grazing-incidence wide-angle X-ray scattering (GIWAXS), but dry OMIECs do not always map well to the real operating conditions.[26] This discrepancy has two origins. First, the lack of an electrolyte obscures the real operational state. Second, there are time-dependent relaxation effects after the bias is removed and films are removed from the solution, especially for n-type materials but also relevant for p-type materials. Thus, it is critical to rational material design that in situ/in operando techniques be developed to characterize OMIECs in contact with the electrolyte and with active potential application.[27]

In situ X-ray scattering of electrified interfaces, under potential control and in contact with the electrolyte, has an extensive history for hard X-ray scattering of inorganic interfaces.[28] Typical designs are of a plunger[29] or inflatable window design.[30−32] The key tradeoff in the design of in situ X-ray scattering cells involves having adequate solution access to the interface of interest to enable electrochemical switching (by minimizing series resistance) while reducing the electrolyte path length to minimize the interference from the amorphous halo of the (typically aqueous) electrolyte. To effectively study doping in semicrystalline polymer materials, it is critical to be able to access the $\pi-\pi$ stacking feature, typically at $\approx$1.7 $Å^{-1}$, and the lamella scattering feature, typically $\approx$0.3 $Å^{-1}$, at device-relevant thicknesses ($\approx$100 nm) while in contact with the electrolyte. Unfortunately, the $\pi-\pi$ feature often lies directly in the region of water scattering. Here, we highlight recent designs for in situ X-ray studies of OMIECs. All designs are based on grazing-incidence configurations due to the weak scattering by the thin polymer films. Bischak et al. designed an inverted geometry where the X-ray probes through a thin gold substrate in contact with the electrolyte on the far side. This provided potential control and electrolyte contact, but the unwanted scattering/absorption of the Kapton/gold obscured access to the $\pi-\pi$ feature.[33] Paulsen et al. presented a "cone cell" that radially limits the extent of the electrolyte (and thus the path length); however, clear observation of the film $\pi-\pi$ stacking required film thickness similar to the X-ray beam height (μm) for clear contrast. Recently, a cell based on a porous (frit) substrate has been presented that allows free X-ray access to all peaks of interest by allowing direct contact with the electrolyte only from the bottom of the film.[34] The frit design is conceptually simple but requires humidity control on the nonelectrolyte film face and transfer of the films from nonporous substrates and exhibits electrochemical non-idealities from the stainless steel frit. Similar to the frit design, studies have been performed with films on top of polymeric electrolytes[19] in a reflection configuration, eliminating electrolyte swelling but allowing potential-controlled doping. Each of these represents a valuable contribution to the field but suffers certain limitations including a lack of access to the $\pi-\pi$ scattering feature, a requirement of unusually thick films ($\approx\mu$m), difficult/abnormal film preparation, or ill-defined potential.

In this report, we present an approach for in situ studies of OMIEC films based on a simple modification of a low-angle blade coater, commonly used for real-time studies of film formation from a solution.[35] We apply it to the study of the electrochemical doping of poly(3-{[2-(2-methoxyethoxy)-ethoxy]methyl}thiophene-2,5-diyl) (P3MEEMT, see Figure 1A), a recently introduced semicrystalline polymeric OMIEC, based on the regioregular polythiophene backbone of P3HT, distinguished by the presence of hydrophilic oligoethylene oxide (oEG) side chains. In earlier studies,[10] P3MEEMT exhibits a material figure[36] of merit, μC^*, where C^* is the volumetric capacitance, of 49 F/(cm V s) in KCl, on par with ethylene glycol-treated poly(3,4-ethylenedioxythiophene):poly(styrenesulfonate), PEDOT:PSS.[36] To achieve high doping levels, we focus on hexafluorophosphate (PF_6^-) as the counterion[10,21,37] but complement the study with the more biologically relevant Cl^-.

RESULTS AND DISCUSSION

Figure 1 shows a schematic of our system. Conceptually, it is similar to a scanning electrochemical cell[38] and we refer to it here as a "rolling drop" electrode. The electrolyte of interest is trapped between the film (cast on a p++ silicon substrate that acts as the working electrode) and the blade of a low-angle blade coater.[39] The underside of the glass blade is silver-coated and converted to Ag/AgCl by exposure to bleach to serve as both the counter- and quasi-reference in a two-electrode configuration. Thus, the application of the desired potential across the film is nominally identical to the conditions of OECT device testing with standard Ag/AgCl pellet gate electrodes. A typical measurement cycle consists of placing the drop-covered sample at the position of the incident beam for a grazing-incidence wide (or small)-angle scattering measurement. Potential is applied and the system is allowed to achieve a steady state (typically 60−120 s). While the blade is directly over the X-ray spot, the shadow of the blade on the detector prevents out-of-plane X-ray measurements (Figure 1A). This is addressed by translating the blade laterally away from the measurement spot (Figure 1B) while continuously collecting scattering patterns (at 10. Hz in this study), allowing access to a full $\pi/2$ scattering angle. As the blade translates, the meniscus of the electrolyte passes over the measurement spot, effectively tuning the electrolyte thickness in time. In practice, this is done as a kinetic sweep: the drop is translated completely off the X-ray measurement spot, going from fully hydrated (in contact with bulk electrolyte) to nominally dry (in contact with room relative humidity) (Figure 1C). To date, all materials studied with this method (more than ten different modified organic semiconductors) are sufficiently hydrophobic that the drop stays attached to the receding blade and a wetted film is not created. However, it does require that the film be stable to the transit of the air−electrolyte interface. We have found that, in general, polar side-chain polymer films are prone to delamination from the substrate, but a moderate (75 °C for 20 min) anneal creates adequate adhesion to perform the rolling drop measurement. Simultaneously, we collect normal-

https://doi.org/10.1021/acsami.2c06169
ACS Appl. Mater. Interfaces 2022, 14, 29052−29060

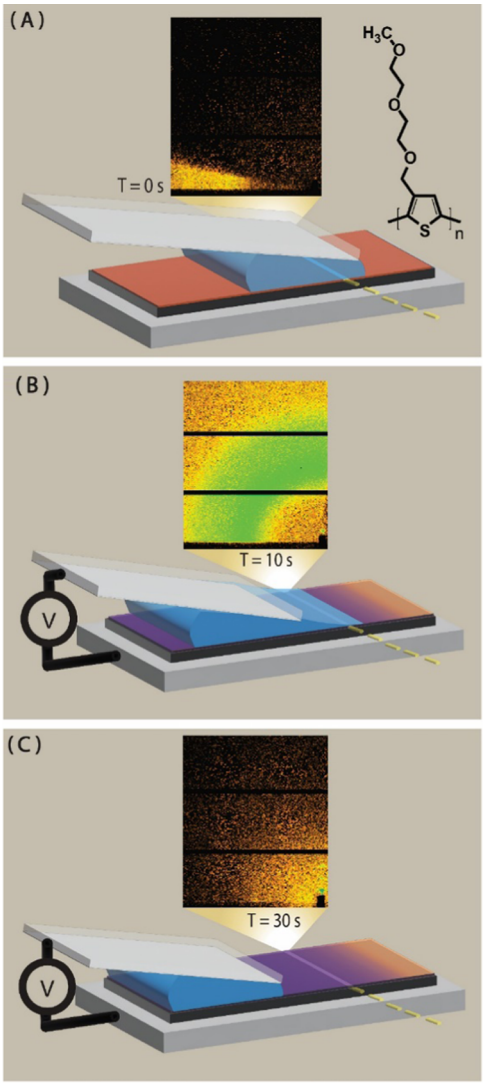

Figure 1. A through C: schematic of the operation of the "rolling drop" electrode, following the dynamic reduction of the electrolyte layer thickness after establishing a steady state. Two-dimensional (2D) images are typical wide-angle X-ray scattering patterns. The blade angle (≈5°) has been exaggerated in the schematic. (A) Initial condition, the blade shadows the out-of-plane scattering. Inset: structure of P3MEEMT. (B) Early times, the blade no longer shadows out-of-plane scattering, but significant electrolyte thickness contributes an amorphous halo to the scattering. (C) Late times, the meniscus has completely passed the measurement area and the sample is dry (in contact with room relative humidity).

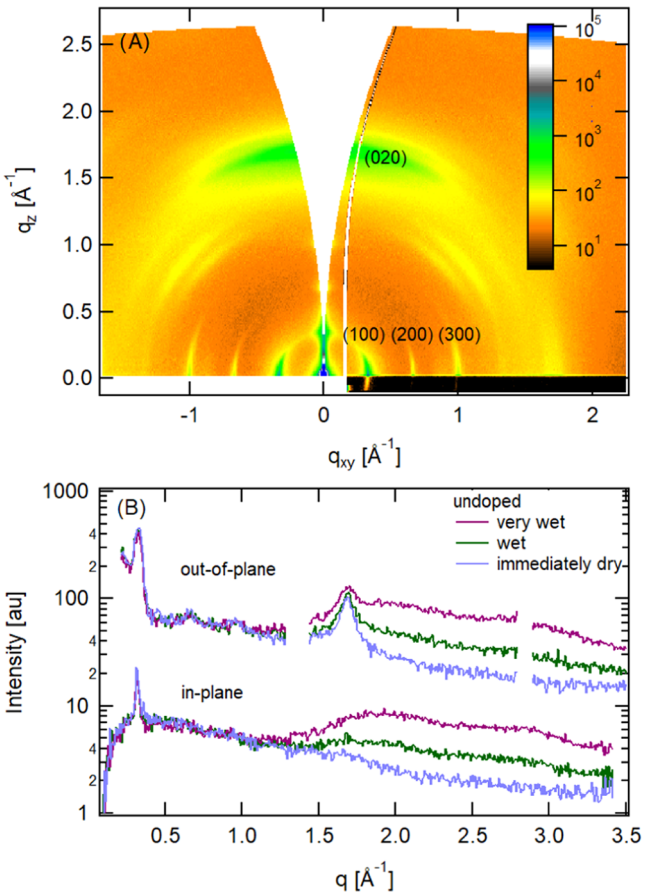

Figure 2. (A) Ex situ GIWAXS pattern from P3MEEMT; in-plane (h00) series and out-of-plane (020) of the face-on material are labeled. (B) In-plane and out-of-plane sector cut from select stages of the drop transit through the X-ray beam. Broad scattering at (≈1.8 and ≈2.8 Å^{-1}) is due to water.

incidence visible reflectance data as a direct measurement of both doping state and swelling.

Using this rolling drop configuration, we comprehensively examine the swelling of the lattice of P3MEEMT. Figure 2A shows the 2D GIWAXS pattern for high number-average molar mass (M_n, 78 kg/mol) P3MEEMT (dispersity, M_w/M_n, 1.47), annealed at 115 °C. These conditions result in textured films with a bimodal distribution of predominantly face-on lamellar crystals with highly ordered (relatively sharp) diffraction features. While the crystal structure of P3MEEMT is not known, we will adopt a notation consistent with the reported $P2_1/c$ unit cell for P3HT.[40] Due to the two chains in the unit cell, the first nonzero $\pi-\pi$ diffraction feature is (020). We note in passing that for films with the c-axis in-plane (as are formed here, confirmed by ellipsometry Figure S1), the out-of-plane (020) has no interference from a possible (001), unlike the commonly observed in-plane feature for edge-on P3HT.[41] We will adopt the notation of q_{hkl}, where h, k, and l are Miller planes indices, when referring to the q-space position of diffraction features.

We first focus on the changes in the polymer upon exposure to the electrolyte (passive swelling) in the neutral state. We have performed complementary studies of the bulk volumetric swelling via spectroscopic ellipsometry in contact with controlled relative humidity (RH, Figures S2 and S3) and liquid water (Figure S4). Nominally, 100% RH results in ≈10% thickness swelling, while contact with the liquid results in ≈18% swelling, an example of Schroeder's paradox.[42,43] Liquid swelling is consistent with values previously reported.[10] Figure 2B shows the select diffraction sector cuts from the time-domain evolution of an undoped film during one kinetic blade passage, highlighting three peaks of interest: the in-plane lamella (100), the out-of-plane π (020), and the broad water scattering feature. Full kinetic results are shown in Figure S5. At early times (Figure 1A), the blade obscures the out-of-plane scattering pattern. As the blade shadow withdraws and the film is still in direct electrolyte contact (Figure 1B, red trace in Figure 2B), the in-plane lamellae are easily visible because they do not overlap with the amorphous halo of water scattering. However, the broad water scattering feature obscures the

https://doi.org/10.1021/acsami.2c06169
ACS Appl. Mater. Interfaces 2022, 14, 29052−29060

(020) peak. By choosing a time when the electrolyte is still present but thin (green trace in Figure 2B), we can analyze the peak position while the film is in contact with the electrolyte, but the peak is strong enough above the background to reliably analyze its position. Finally, as the blade withdraws to its furthest extent (millimeters beyond the X-ray measurements spot), we see a "dry" spectrum (Figure 1C, blue in Figure 2B). Here, the film is in equilibrium with room humidity, which gives the strongest GIWAXS peaks but loses the electrolyte effect as seen by the slight contraction in the (100) direction (see Figure 3B). By careful choice of the time window averaged, we can extract the swollen lattice parameters with high fidelity as well as contrast them with the dry state of the film. We note that, while the rolling drop is removed from the measurement region in the retracted position, lateral conductivity in the film appears sufficient to maintain the nominally dry, doped state. This is confirmed by studies with 0.1 mol/L KCl as the electrolyte. We found that Cl^--doped films were unstable, spontaneously dedoping in about 5 min, as observed by a visible color change and both ex situ ellipsometry and ex situ GIWAXS (Figure S6). However, clear evidence of the doped state is observed in both white-light interferometry (Figure S17) and GIWAXS (Figures S15 and S16) in the rolling drop experiment, with the drop a few millimeters from the measurement region.

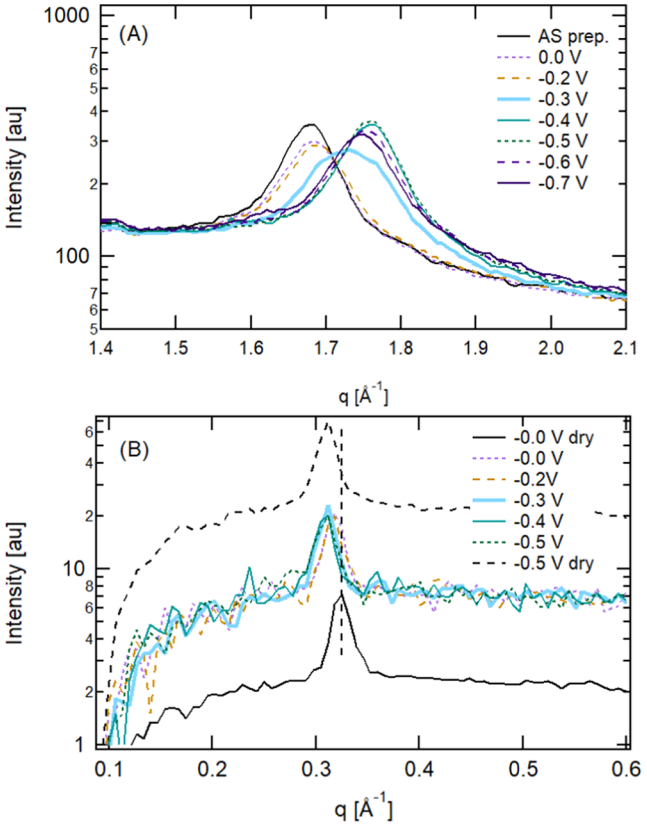

Figure 3. (A) Detail of the out-of-plane (020) feature vs applied potential (vs Ag/AgCl, uncorrected) in 0.1 mol/L KPF_6. Note the absence of an isosbestic point. (B) Detail of the in-plane (100) feature vs applied potential. Colors denote films in contact with the electrolyte (wet); black lines are films with the electrolyte removed (room RH). Note both the subtle swelling by hydration and by doping.

Unlike volumetric swelling, there was no significant difference in q_{100} swelling in ≈100% RH (Figure S7 and Table S1) or liquid water (Figure 2). In both cases, only a 3−4% expansion of the lattice is observed. Notably for P3MEEMT, under all conditions (RH, liquid, and doping level, see below), there is no distinguishable change in the q_{020} associated with the presence of the electrolyte, i.e., there is no detectable electrolyte swelling of the $\pi-\pi$ stacking. Additionally, there is no significant change in crystalline order, as reflected in either the diffraction widths or amplitudes, indicating that the electrolyte does not disrupt or enhance the existing crystal structure. The change in the q_{100} of 3−4% is significantly smaller than the film volumetric swelling (10−18%), clearly establishing that the majority of the volumetric expansion occurs in the amorphous regions of the film. Assuming the $P2_1/c$ structure with two chains per unit cell (four thiophenes) proposed for P3HT,[40] and no changes in the crystal angles upon swelling, the undoped unit cell volume increases by ≈40 Å^3 in contact with the electrolyte. This corresponds to ≈1/3 of a water molecule (30 Å^3) per monomer. Thus, despite the polarity of the side chains, the crystalline regions are relatively hydrophobic in the neutral state. We note that the incompressibility assumption may underestimate the amount of water in the side chains due to the conformation flexibility of the side chains.

Next, we present the effect of potential on the lattice, as shown in Figure 3. This is done as subsequent blade passages with a different potential for each blade passage. We first focus on the behavior of q_{020}. As is often observed for doped P3HT,[19,44,45] the q_{020} is observed to increase, indicating a contraction of $\pi-\pi$ separation above a critical potential/induced charge density. As there is no evidence for changes in the (020) due to electrolyte swelling, here, we analyze films

Table 1. Comparison of Characteristic Diffraction Features upon Hydration and Doping with 0.1 mol/L KPF_6 at −0.5 V Relative to Ag/AgCl[a]

	dry (q/Å^{-1})	change (%)	wet (q/Å^{-1})	dry (FWHM/Å^{-1})	change (%)	wet (FWHM/Å^{-1})
(100)						
undoped	0.331 ± 0.001	−3 ± 1	0.322 ± 0.004	0.018	0	0.018
% change	−3 ± 1		−2 ± 1	0		0
doped	0.322 ± 0.001	−2 ± 1	0.314 ± 0.001	0.018	0	0.018
(020)						
undoped	1.683 ± 0.002	0 ± 1	1.684 ± 0.002	0.097	1 ± 4	0.098
% change	3 ± 1		3 ± 1	2 ± 4		1 ± 4
doped	1.758 ± 0.002	0 ± 1	1.757 ± 0.002	0.095	2 ± 4	0.097

[a]Uncertainties are 1 standard deviation based on the covariance matrix of the peak fits.

https://doi.org/10.1021/acsami.2c06169
ACS Appl. Mater. Interfaces 2022, 14, 29052−29060

with minimal electrolyte interference for high quality, as shown in Figure 3. There is no clear isosbestic point in the data, implying that at intermediate potentials (−0.30 V vs Ag/AgCl) the system evolves as a continuous alloy, not as distinct undoped and doped phases.[33] We note that to maintain a consistent sign convention between the in situ studies and OECT device studies (see below), we report all potentials relative to a Ag/AgCl quasi-reference with the film grounded. From Figure 3A, it is apparent that there are no significant changes in either relative (020) crystallinity or crystal size (coherence length) with doping. Diffraction feature widths from line fits are presented in Table S2. This is in contrast to reports of enhanced ordering upon doping of regiorandom P3HT.[41] The face-on crystals in these films (annealed at 115 °C) exhibit high levels of order as prepared: the (100) coherence length, $l_c = 2\pi/\text{FWHM}$ (FWHM = full width at half-maximum), can exceed 30 nm, while the (020) l_c can exceed 8 nm; therefore, additional ordering may not be detectable. Unfortunately, studies of unannealed films, with lower initial orders, were confounded by delamination.

Figure 3B shows the evolution of the (100). In contrast to the q_{020} contraction, a small ≈3% expansion of the lamella is observed, again at ≈ −0.3 V. This is in addition to the ≈3% expansion due to the electrolyte, such that the doped, swollen film expands a total of ≈5%.

Using the rolling drop electrode, we are able to, at the same exact location of a single film, characterize four distinct conditions: undoped vs doped, dry (room relative humidity ≈35%) vs in contact with the liquid (wet). In Table 1, we summarize the behavior of the face on crystals (in-plane lamella (100) and out-of-plane $\pi-\pi$ (020)) for these four states and the relative changes upon doping and swelling. The prominent observation in lattice spacing is a sharp contraction of the $\pi-\pi$ spacing of 3% at −0.2 V, accompanied by a 2−3% expansion of the lamella separation, $d_{100} \equiv 2\pi/q_{100}$. The very small doping-induced change in the q_{100} implies that, contrary to the ≈3% change in the undoped unit cell volume upon hydration, the volume of the unit cell does not change significantly upon doping; the small additional (100) expansion is compensated by the (020) contraction. The dry film expands immeasurably, while the wet film *contracts* by 25 Å^3, as compared with a PF_6^- ionic volume of 65 Å^3.

In Figure 4, we compare the structural metrics (q_{100} and q_{020}) as a function of applied potential with device data from independently characterized OECTs (see Figures S8−S11). We use normal-incidence white-light-interferometry recorded simultaneously with in situ GIWAXS and spectroscopic ellipsometry recorded contemporaneously with the device measurements to ensure comparison at the same doping level (Figures S12 and S13). We find that a nominal 0.1 V offset must be applied to the in situ GIWAXS potential to agree with the device data. This shift has been applied to the diffraction data in Figure 4. We attribute this to trace oxidation of the polymer depending on casting solution age and not to differences in the Ag/AgCl reference (pellet vs thin film). While the $\pi-\pi$ spacing is invariant with increased doping above a threshold, the d_{100} appears to relax (deswell) at higher injected charge densities. This deswelling is also observed for the out-of-plane (100) (see Figure S14), but it is not observed in KCl (see Figure S15). However, one cannot achieve as high as injected charge density in KCl. Similar deswelling at high charging has been reported for PEDOT:PSS[26] and might be

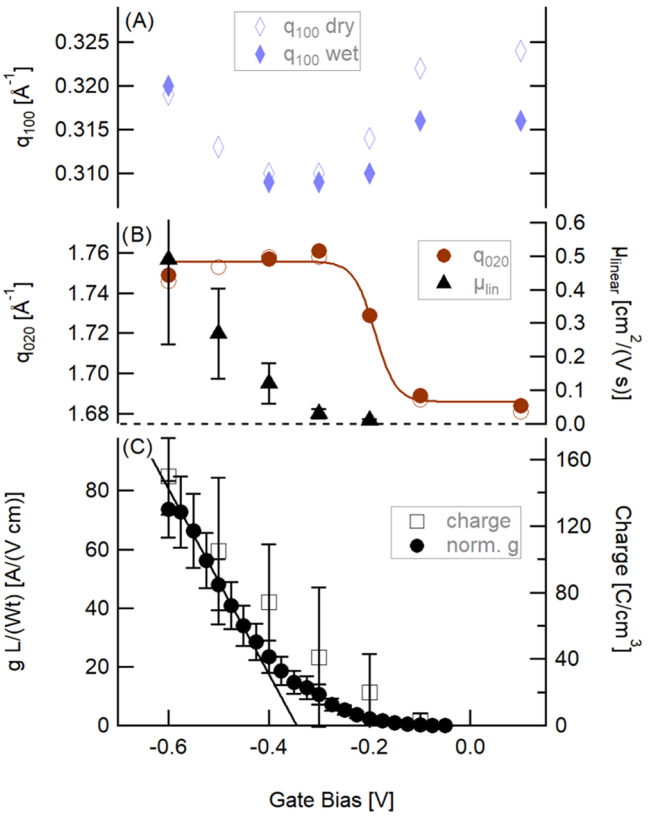

Figure 4. (A) Hydrated/wet (closed) and dry (open) scattering magnitude for the q_{100} (blue) and (B) q_{020} (red) features as a function of gate bias showing the lamellar expansion (decrease in q_{100}) and pi contraction (increase in q_{020}) as the film is oxidized. The line is a sigmoid-fit guide to the eye. (C) Also shown are the linear mobility, the normalized transconductance [g L/(Wt)] averaged over eight devices from OECTs with thickness ranging from 74 to 114 nm and channel length ranging from 82 to 397 μm, and the charge-per-unit volume from chronocoulometry. The GIWAXS potential has been corrected as described in the text.

reflective of bipolaron formation, although beam damage of the highly doped film cannot be excluded.

There have been extensive studies, both ex situ and in situ, of P3HT doped with either bis(trifluoromethane)sulfonimide, TFSI, or 2,3,5,6-tetrafluoro-7,7,8,8-tetracyanoquinodimethane, F4TCNQ, either by vapor or solvent exchange or with polymer electrolytes, so effectively "dry." Common to all studies is a contraction of the $\pi-\pi$ and expansion of the lamella above some critical doping/charging level. The work most directly comparable to the present study is that of Thomas et al.,[19] who used a polymer electrolyte (thus prohibiting electrolyte swelling) to enable TFSI doping of P3HT. They report a sharp 4% contraction of (020) at a charge density of ≈5×10^{20} h/cm^3 (h = hole) or 95 C/cm^3, similar to the ≈40 C/cm^3 accumulated charge at −0.2 V (corrected), as shown in Figure 4. However, unlike the negligible volumetric swelling observed with PF_6^- in P3MEEMT in the presence of the electrolyte, TFSI doping results in a 12% expansion of (100) in P3HT and an ≈80 Å^3 increase in the unit cell volume. In the work of Thomas et al., the crystal changes ($\pi-\pi$ contraction and (100) expansion) were attributed to a phase change due to the ingress of dopant ions above a critical charging density. Importantly, the crystal structure change is directly correlated with a steplike increase in film mobility. As discussed in the

https://doi.org/10.1021/acsami.2c06169
ACS Appl. Mater. Interfaces 2022, 14, 29052−29060

Introduction section, the mobility of polythiophenes generally increases exponentially with increasing doping levels and plateaus at charge levels ≈5 × 10^{20} h/cm^3.[46] In Figure 4, it is clear that, while the crystal morphology changes at a potential similar to the transistor threshold, the device mobility is still increasing significantly beyond the saturation of changes in the crystal structure. This suggests that transport in the P3MEEMT devices is more influenced by the amorphous domains, relative to the previous studies of P3HT. We note that, while P3MEEMT films clearly contain highly oriented material, GIWAXS does not provide absolute crystallinity. Thus, the crystal fraction in P3MEEMT may be less than the typical 50% found in P3HT.[47] The evolution of the total film charge, monotonically increasing throughout the studied potential range, and the in situ GIWAXS, saturating at moderate potential, is consistent with the observation of Thomas et al.[19] that doping initially modifies the crystals (polarons are more stable in the highly ordered material) and subsequently dopes the amorphous material. Unlike P3HT, this cannot be confirmed by spectroelectrochemistry, as there are no distinct features (vibronic progression) attributable to the crystalline P3MEEMT.[10]

Figures S15 and S16 show the comparable data for doping in 0.1 mol/L KCl. Consistent with earlier reports of device threshold shifts,[10] the KCl-doped crystals change at nominally 200 mV deeper potentials. Except for the potential shift, there are no significant differences in either the hydration- or doping-induced structural changes between KPF_6 and KCl electrolytes. It is notable that there is no significant difference in the crystal volumetric swelling between PF_6^- (Figures 3 and S14) and Cl^-. In studies of total mass uptake by QCM,[10] it was noted that films took up nominally seven water molecules for each Cl^- or an "active swelling" of ≈10% by mass in addition to the passive swelling of ≈20%. There is no evidence for increased electrolyte uptake for the Cl^--doped crystalline material, emphasizing the relatively hydrophobic nature of the crystals. Similarly, based on QCM,[10] PF_6^- is a dehydrating (hydrophobic) ion, leading to mass loss upon doping due to water ejection from the passively swollen film.[10] It is unambiguous that the crystalline material, whether doped with Cl^- or PF_6^-, does not exhibit significant "active" or additional, bias-driven swelling. This is in dramatic contrast to the bulk of many OMIEC films that are known to swell up to 100% in response to doping[23] and frame swelling of OECTs as a complicated effect that varies widely between the amorphous and crystalline fractions of films. It is also notable that, unlike the case of TSFI in P3HT (12% expansion of lamella)[19] or F4TCNQ in P3HT (11% expansion of the lamella),[48] there is little (≈3% expansion) change in the lamella upon incorporation of PF_6^-, in spite of similar ion volumes and doping levels. This suggests that the (presumed mostly amorphous) oEG side chains of P3MEEMT may be more conformationally forgiving and are capable of accommodating the strain from both the ion volume and the 3% compression in the $\pi-\pi$ direction more readily than the shorter alkyl of P3HT. It is interesting to note that for in-plane q_{100}, the swelling of the PF_6^--doped film by the electrolyte is undetectable; however, this trend is not reflected in the out-of-plane q_{100} (see Figure S14). Whether this is reflective of confinement in the face-on crystals or spurious correlation in the subtle data cannot be determined.

CONCLUSIONS

In this manuscript, we introduce a novel method for observing the crystal lattice of OMIECs in direct contact with electrolyte and potential by modifying a commonly used blade coater. With each blade passage, we interrogate the electrolyte swollen crystal lattice and the dry lattice at a given potential. Using this method, we can extract both the hydrated and dry lattice parameters, both in- and out-of-plane. By performing kinetic traces at multiple potentials, we can separate the effect of electrolyte swelling from that of the bias-driven swelling. For P3MEEMT, we observe minimal (<5%) crystal swelling compared to the bulk (≈20%) swelling of the film, implying that the electrolyte predominantly resides in the amorphous content of the film. The doping-induced changes in the crystal structure, contraction in the $\pi-\pi$ direction and expansion of the lamella separation with negligible change in crystal volume, saturate well before either the total film charge or device mobility. Overall, this technique provides unique insights into the swollen structure of OMIECs and has a valuable role in the suit of characterization techniques that have been developed.

EXPERIMENTAL SECTION

Material and Film Deposition. Poly(3-{[2-(2-methoxyethoxy)-ethoxy]methyl}thiophene-2,5-diyl), P3MEEMT, was synthesized as described previously.[10] Based on high-performance liquid chromatography in tetrahydrofuran, the number-average molar mass (M_n) was 78 kg/mol and the mass-average molar mass (M_w) was 115 kg/mol, with dispersity, M_w/M_n, of 1.47. All electrolyte solutions were prepared with 18 MΩ Millipore water. KCl from Sigma and KPF_6 provided by Dr. Thomas Moffat were used as received.

All substrates (p++-doped silicon for X-ray diffraction or ellipsometry, glass for devices) were cleaned by 10 min ultrasonic agitation in each of chloroform and isopropyl alcohol, followed by ultraviolet−ozone treatment for 10 min. P3MEEMT was deposited by blade coating with a custom, low-angle coater described in ref 39. The blade height was 200 μm, and the blade speed was nominally 40 mm/s. The substrate temperature was 30 °C. The blade speed was varied to produce variable film thicknesses. The solution was 20 mg/mL in chlorobenzene. The solution was dissolved at 50 °C with stirring and allowed to cool to room temperature. The typical film thickness was 75 nm.

Organic Electrochemical Devices. OECT devices were prepared on Au bottom contact devices with nominal channel lengths of 100, 200, 300, or 400 μm and channel widths of 1 mm, created by vapor deposition through a shadow mask on a glass substrate. Nominally, 50 nm of Au was deposited on a 10 nm Cr adhesion layer. After deposition of the polymer film, excess material was removed by manual scrubbing to limit the material to the nominal channel region. A polydimethylsiloxane well was adhered to the chip and filled with ≈350 μL of electrolyte. A Ag/AgCl pellet electrode was used as the gate. A Keithley 2632 dual-channel source meter was used to record the gate and drain currents as a function of gate and source potentials. μC^* and Vth were obtained from the saturation characteristics of the numerically computed transconductance

$$g = \frac{\mathrm{d}\, I_D}{\mathrm{d}\, V_{GS}} = \mu C^* \frac{W\, t}{L}(V\mathrm{th} - V_{GS})$$

where I_D is the drain current, V_{GS} is the gate potential, Vth is the threshold voltage, C^* is the volumetric capacitance, μ is the mobility, W is the channel width, t is the film thickness, and L is the channel length. The film thickness was determined by spectroscopic ellipsometry (in the dry state) and the channel dimensions were determined by optical microscopy, for each device.

In the linear regime, the channel current is given by

$$I_D = \rho\mu \frac{W\, t}{L} V_{DS}$$

https://doi.org/10.1021/acsami.2c06169
ACS Appl. Mater. Interfaces 2022, 14, 29052−29060

where ρ is the charge in the channel and V_{DS} is the applied voltage. Linear mobilities were extracted from the gate-current-corrected, low-V_{DS} region of output curves at $V_{GS} \geq 0.2$ V.

Chronocoulometry. The charge density in the film was determined by integrated chronocoulometry based on measured film area following the procedures of ref 37.

Grazing-Incidence Wide-Angle X-ray scattering (GIWAXS). GIWAXS was performed at the 11-BM CMS beamline at NSLS-II. A beam energy of 13.5 keV was used for all measurements. The sample-to-detector distance and beam center were determined from a silver behenate standard. The vertical center was shifted to produce out-of-plane (h00) series with no extrapolated offset. This empirically corrects for both the shift in the incident pointing vector due to the standing wave at grazing-incidence and for the refractive index correction upon exit. Ex situ data was taken with a Pilatus 800K detector, with the sample in vacuum. In situ data (both rolling drop and solvent vapor annealing) was taken in air with a Pilatus 300K detector. Solvent vapor annealing was done in a custom cell, sealed with Kapton windows, kindly provided by Dr. Ben Ocko. The cell allowed up to nine samples to be measured in parallel. Water vapor was controlled by a mixed stream of pure nitrogen and nitrogen saturated with water vapor via a bubbler. A very large volume bubbler was used to limit the evaporative cooling of the liquid water. The relative humidity was recorded by a sensor in the cell and consistent with vapor flow mixing rates and 100% saturation.

Rolling drop GIWAXS was performed as described in the main text. Typically, 300 nm of Ag was deposited on a glass slide (blade) with a 10 nm Cr adhesion layer and converted to Ag/AgCl by exposure to 4% bleach for 2 min. The blade−sample gap was typically 300 μm, and nominally, 500 μL of electrolyte was dispensed between the blade and substrate to form the drop. The blade−sample potential was controlled by an EG&G PAR 363 potentiostat, under analog control by custom software developed by NSLS-II.

Spectroscopic Ellipsometry (SE). SE was performed with a JA Woollam Co M2000-D spectroscopic instrument, nominally spanning 200−1700 nm. A custom cell was used for both vapor exposure and liquid exposure. The long liquid path length limited the wavelength range to nominally 300−1000 nm. Water vapor was controlled by a mixed stream of pure nitrogen and nitrogen saturated with water vapor via a bubbler. Relative humidity was recorded by a sensor in the cell and consistent with vapor flow mixing rates and an RH of 98−99% at saturation. CompleteEase software was used to correct for any birefringence of the cell windows and for analysis. For SVA, a uniaxial model was fit to the initial, dry film, and then, all subsequent data were fitted to an EMA mixture of the dry dielectric function and water, allowing volume fraction and thickness to independently vary.

White-Light Interferometry (WLI). Concurrent with the rolling drop GIWAXS measurements, WLI was performed at normal incidence on the same spot on the sample as the diffraction measurements when the drop had cleared and there was no obstruction. This provides immediate feedback on the doping of the film. The custom system is based on a 6 around 1 fiber bundle for illumination/collection, a deuterium/quartz-tungsten halogen broad-band source, and a Si diode-array detector. The reflectance spectra, corrected by reference to the reflection from a native oxide-covered Si chip, were analyzed by CompleteEase software.

■ ASSOCIATED CONTENT

Supporting Information

The Supporting Information is available free of charge at https://pubs.acs.org/doi/10.1021/acsami.2c06169.

Figures S1−S17, Tables S1, and S2; example time-dependent GIWAXS following transit of the electrolyte drop, dielectric functions of the P3MEEMT films, in situ ellipsometry analysis of film swelling, GIWAXS as a function of relative humidity, output and transfer curves of typical OECTs, linear mobility analysis, comparison of charge density with dielectric function, linear mobility vs charge density, normal-incidence reflectance vs applied potential, summary results for films annealed at 115 °C in 0.1 mol/L KPF_6 and 115° in 0.1 mol/L KCl, and tabulated diffraction feature positions and widths as a function of relative humidity and doping potential (PDF)

■ AUTHOR INFORMATION

Corresponding Author

Lee J. Richter − *Materials Science and Engineering Division, National Institute of Standards and Technology, Gaithersburg, Maryland 20899, United States;* orcid.org/0000-0002-9433-3724; Email: lee.richter@nist.gov

Authors

Lucas Q. Flagg − *Materials Science and Engineering Division, National Institute of Standards and Technology, Gaithersburg, Maryland 20899, United States;* orcid.org/0000-0002-2798-5650

Lauren E. Asselta − *Materials Science and Engineering Division, National Institute of Standards and Technology, Gaithersburg, Maryland 20899, United States*

Nicholas D'Antona − *Materials Science and Engineering Division, National Institute of Standards and Technology, Gaithersburg, Maryland 20899, United States*

Tommaso Nicolini − *Université de Bordeaux, CNRS Bordeaux INP/ENSCBP, Laboratoire de Chimie de Polymères Organiques UMR 5629, 33615 Pessac, France;* orcid.org/0000-0002-9218-4702

Natalie Stingelin − *Université de Bordeaux, CNRS Bordeaux INP/ENSCBP, Laboratoire de Chimie de Polymères Organiques UMR 5629, 33615 Pessac, France; School of Materials Science & Engineering and School of Chemical & Biomolecular Engineering, Georgia Institute of Technology, Atlanta, Georgia 30318, United States*

Jonathan W. Onorato − *Department of Materials Science and Engineering, University of Washington, Seattle, Washington 98195, United States*

Christine K. Luscombe − *pi-Conjugated Polymers Unit, Okinawa Institute of Science and Technology Graduate University, Kunigami-gun, Okinawa 904-0495, Japan;* orcid.org/0000-0001-7456-1343

Ruipeng Li − *National Synchrotron Light Source II, Brookhaven National Laboratory, Upton, New York 11973, United States*

Complete contact information is available at: https://pubs.acs.org/10.1021/acsami.2c06169

Notes

The authors declare no competing financial interest.

■ ACKNOWLEDGMENTS

L.Q.F. acknowledges the support of a NIST-National Research Council fellowship. L.E.A. acknowledges a NIST-Montgomery College internship. N.D'A. acknowledges a NIST summer undergraduate research fellowship. J.W.O. acknowledges the National Science Foundation (NSF) CBET-1922259 for support. This research used beamline 11-BM (CMS) of the National Synchrotron Light Source, a U.S. Department of Energy (DOE) Office of Science User Facility operated for the DOE Office of Science by Brookhaven National Laboratory under contract no. DE-SC0012704. The authors thank Sara

https://doi.org/10.1021/acsami.2c06169
ACS Appl. Mater. Interfaces 2022, 14, 29052−29060

Orski for size-exclusion chromatography studies of P3MEEMT. T.N. and N.S.-S. are grateful for the financial support provided by the IONBIKE RISE project, which has received funding from the European Union's Horizon 2020 Research and Innovation Program under Horizon 2020 RISE Marie Skłodowska-Curie grant agreement no. 823 989. T.N. and N.S.-S. also acknowledge funding from the MARBLE project, supported by the Excellence Initiative by due University of Bordeaux (IDEX Bordeaux).

REFERENCES

(1) Rivnay, J.; Inal, S.; Salleo, A.; Owens, R. M.; Berggren, M.; Malliaras, G. G. Organic Electrochemical Transistors. *Nat. Rev. Mater.* **2018**, *3*, No. 17086.
(2) Paulsen, B. D.; Fabiano, S.; Rivnay, J. Mixed Ionic-Electronic Transport in Polymers. *Annu. Rev. Mater. Res.* **2021**, 73−99.
(3) Moser, M.; Ponder, J. F.; Wadsworth, A.; Giovannitti, A.; McCulloch, I. Materials in Organic Electrochemical Transistors for Bioelectronic Applications: Past, Present, and Future. *Adv. Funct. Mater.* **2019**, *29*, No. 1807033.
(4) Guo, K.; Wustoni, S.; Koklu, A.; Díaz-Galicia, E.; Moser, M.; Hama, A.; Alqahtani, A. A.; Ahmad, A. N.; Alhamlan, F. S.; Shuaib, M.; Pain, A.; McCulloch, I.; Arold, S. T.; Grünberg, R.; Inal, S. Rapid Single-Molecule Detection of COVID-19 and MERS Antigens via Nanobody-Functionalized Organic Electrochemical Transistors. *Nat. Biomed. Eng.* **2021**, *5*, 666−677.
(5) Nawaz, A.; Liu, Q.; Leong, W. L.; Fairfull-Smith, K. E.; Sonar, P. Organic Electrochemical Transistors for In Vivo Bioelectronics. *Adv. Mater.* **2021**, *33*, No. 2101874.
(6) Moia, D.; Giovannitti, A.; Szumska, A. A.; Schnurr, M.; Rezasoltani, E.; Maria, I. P.; Barnes, P. R. F.; McCulloch, I.; Nelson, J.*A Salt Water Battery with High Stability and Charging Rates Made from Solution Processed Conjugated Polymers with Polar Side Chains*, 2017, pp 1−62.
(7) Tan, S. T. M.; Quill, T. J.; Moser, M.; LeCroy, G.; Chen, X.; Wu, Y.; Takacs, C. J.; Salleo, A.; Giovannitti, A. Redox-Active Polymers Designed for the Circular Economy of Energy Storage Devices. *ACS Energy Lett.* **2021**, *6*, 3450−3457.
(8) van de Burgt, Y.; Melianas, A.; Keene, S. T.; Malliaras, G.; Salleo, A. Organic Electronics for Neuromorphic Computing. *Nat. Electron.* **2018**, *1*, 386−397.
(9) Ji, X.; Paulsen, B. D.; Chik, G. K. K.; Wu, R.; Yin, Y.; Chan, P. K. L.; Rivnay, J. Mimicking Associative Learning Using an Ion-Trapping Non-Volatile Synaptic Organic Electrochemical Transistor. *Nat. Commun.* **2021**, *12*, No. 2480.
(10) Flagg, L. Q.; Bischak, C. G.; Onorato, J. W.; Rashid, R. B.; Luscombe, C. K.; Ginger, D. S. Polymer Crystallinity Controls Water Uptake in Glycol Side-Chain Polymer Organic Electrochemical Transistors. *J. Am. Chem. Soc.* **2019**, *141*, 4345−4354.
(11) Giovannitti, A.; Rashid, R. B.; Thiburce, Q.; Paulsen, B. D.; Cendra, C.; Thorley, K.; Moia, D.; Mefford, J. T.; Hanifi, D.; Weiyuan, D.; Moser, M.; Salleo, A.; Nelson, J.; McCulloch, I.; Rivnay, J. Energetic Control of Redox-Active Polymers toward Safe Organic Bioelectronic Materials. *Adv. Mater.* **2020**, *32*, No. 1908047.
(12) Giovannitti, A.; Nielsen, C. B.; Sbircea, D. T.; Inal, S.; Donahue, M.; Niazi, M. R.; Hanifi, D. A.; Amassian, A.; Malliaras, G. G.; Rivnay, J.; McCulloch, I. N-Type Organic Electrochemical Transistors with Stability in Water. *Nat. Commun.* **2016**, *7*, No. 13066.
(13) Noriega, R.; Salleo, A.; Spakowitz, A. J. Chain Conformations Dictate Multiscale Charge Transport Phenomena in Disordered Semiconducting Polymers. *Proc. Natl. Acad. Sci. U.S.A.* **2013**, *110*, 16315−16320.
(14) Venkateshvaran, D.; Nikolka, M.; Sadhanala, A.; Lemaur, V.; Zelazny, M.; Kepa, M.; Hurhangee, M.; Kronemeijer, A. J.; Pecunia, V.; Nasrallah, I.; Romanov, I.; Broch, K.; McCulloch, I.; Emin, D.; Olivier, Y.; Cornil, J.; Beljonne, D.; Sirringhaus, H. Approaching Disorder-Free Transport in High-Mobility Conjugated Polymers. *Nature* **2014**, *515*, 384−388.
(15) Himmelberger, S.; Vandewal, K.; Fei, Z.; Heeney, M.; Salleo, A. Role of Molecular Weight Distribution on Charge Transport in Semiconducting Polymers. *Macromolecules* **2014**, *47*, 7151−7157.
(16) Gu, K.; Snyder, C. R.; Onorato, J.; Luscombe, C. K.; Bosse, A. W.; Loo, Y. L. Assessing the Huang-Brown Description of Tie Chains for Charge Transport in Conjugated Polymers. *ACS Macro Lett.* **2018**, *7*, 1333−1338.
(17) Peterson, K. A.; Thomas, E. M.; Chabinyc, M. L. Thermoelectric Properties of Semiconducting Polymers. *Annu. Rev. Mater. Res.* **2020**, *50*, 551−574.
(18) Kim, S. H.; Hong, K.; Xie, W.; Lee, K. H.; Zhang, S.; Lodge, T. P.; Frisbie, C. D. Electrolyte-Gated Transistors for Organic and Printed Electronics. *Adv. Mater.* **2013**, *25*, 1822−1846.
(19) Thomas, E. M.; Brady, M. A.; Nakayama, H.; Popere, B. C.; Segalman, R. A.; Chabinyc, M. L. X-Ray Scattering Reveals Ion-Induced Microstructural Changes During Electrochemical Gating of Poly(3-Hexylthiophene). *Adv. Funct. Mater.* **2018**, *28*, No. 1803687.
(20) Savva, A.; Cendra, C.; Giugni, A.; Torre, B.; Surgailis, J.; Ohayon, D.; Giovannitti, A.; McCulloch, I.; Di Fabrizio, E.; Salleo, A.; Rivnay, J.; Inal, S. Influence of Water on the Performance of Organic Electrochemical Transistors. *Chem. Mater.* **2019**, *31*, 927−937.
(21) Cendra, C.; Giovannitti, A.; Savva, A.; Venkatraman, V.; McCulloch, I.; Salleo, A.; Inal, S.; Rivnay, J. Role of the Anion on the Transport and Structure of Organic Mixed Conductors. *Adv. Funct. Mater.* **2019**, *29*, No. 1807034.
(22) Flagg, L. Q.; Bischak, C. G.; Quezada, R. J.; Onorato, J. W.; Luscombe, C. K.; Ginger, D. S. P-Type Electrochemical Doping Can Occur by Cation Expulsion in a High-Performing Polymer for Organic Electrochemical Transistors. *ACS Mater. Lett.* **2020**, *2*, 254−260.
(23) Moser, M.; Hidalgo, T. C.; Surgailis, J.; Gladisch, J.; Ghosh, S.; Sheelamanthula, R.; Thiburce, Q.; Giovannitti, A.; Salleo, A.; Gasparini, N.; Wadsworth, A.; Zozoulenko, I.; Berggren, M.; Stavrinidou, E.; Inal, S.; McCulloch, I. Side Chain Redistribution as a Strategy to Boost Organic Electrochemical Transistor Performance and Stability. *Adv. Mater.* **2020**, *32*, No. 2002748.
(24) Bihar, E.; Deng, Y.; Miyake, T.; Saadaoui, M.; Malliaras, G. G.; Rolandi, M. A Disposable Paper Breathalyzer with an Alcohol Sensing Organic Electrochemical Transistor. *Sci. Rep.* **2016**, *6*, No. 27582.
(25) Nicolini, T.; Surgailis, J.; Savva, A.; Scaccabarozzi, A. D.; Nakar, R.; Thuau, D.; Wantz, G.; Richter, L. J.; Dautel, O.; Hadziioannou, G.; Stingelin, N. A Low-Swelling Polymeric Mixed Conductor Operating in Aqueous Electrolytes. *Adv. Mater.* **2021**, *33*, No. 2005723.
(26) Paulsen, B. D.; Wu, R.; Takacs, C. J.; Steinrück, H.; Strzalka, J.; Zhang, Q.; Toney, M. F.; Rivnay, J. Time-Resolved Structural Kinetics of an Organic Mixed Ionic−Electronic Conductor. *Adv. Mater.* **2020**, *32*, No. 2003404.
(27) Wu, R.; Matta, M.; Paulsen, B. D.; Rivnay, J. Operando Characterization of Organic Mixed Ionic/Electronic Conducting Materials. *Chem. Rev.* **2022**, *122*, 4493−4551.
(28) Wu, C. H.; Weatherup, R. S.; Salmeron, M. B. Probing Electrode/Electrolyte Interfaces in Situ by X-Ray Spectroscopies: Old Methods, New Tricks. *Phys. Chem. Chem. Phys.* **2015**, *17*, 30229−30239.
(29) Koop, T.; Schindler, W.; Kazimirov, A.; Scherb, G.; Zegenhagen, J.; Schulz, T.; Feidenhans', R.; Kirschner, J. Electrochemical Cell for in Situ X-Ray Diffraction under Ultrapure Conditions. *Rev. Sci. Instrum.* **1998**, *69*, 1840−1843.
(30) Wang, J.; Ocko, B. M.; Davenport, A. J.; Isaacs, H. S. In Situ X-Ray-Diffraction and -Reflectivity Studies of the Au(111)/Electrolyte Interface: Reconstruction and Anion Adsorption. *Phys. Rev. B* **1992**, *46*, 10321−10338.
(31) Herron, M. E.; Doyle, S. E.; Roberts, K. J.; Robinson, J.; Walsh, F. C. Instrumentation and Cell Design for in Situ Studies of Electrode Surfaces Using X-Ray Synchrotron Radiation. *Rev. Sci. Instrum.* **1992**, *63*, 950−955.

https://doi.org/10.1021/acsami.2c06169
ACS Appl. Mater. Interfaces 2022, 14, 29052−29060

(32) Samant, M. G.; Toney, M. F.; Borges, G. L.; Blum, L.; Melroy, O. R. In-Situ Grazing Incidence X-Ray Diffraction Study of Electrochemically Deposited Pb Monolayers on Ag(111). *Surf. Sci.* **1988**, *193*, L29−L36.
(33) Bischak, C. G.; Flagg, L. Q.; Yan, K.; Rehman, T.; Davies, D. W.; Quezada, R. J.; Onorato, J. W.; Luscombe, C. K.; Diao, Y.; Li, C.-Z. Z.; Ginger, D. S. A Reversible Structural Phase Transition by Electrochemically-Driven Ion Injection into a Conjugated Polymer. *J. Am. Chem. Soc.* **2020**, *142*, 7434−7442.
(34) Paulsen, B. D.; Giovannitti, A.; Wu, R.; Strzalka, J.; Zhang, Q.; Rivnay, J.; Takacs, C. J. Electrochemistry of Thin Films with In Situ/Operando Grazing Incidence X-Ray Scattering: Bypassing Electrolyte Scattering for High Fidelity Time Resolved Studies. *Small* **2021**, *17*, No. 2103213.
(35) Richter, L. J.; Delongchamp, D. M.; Amassian, A. Morphology Development in Solution-Processed Functional Organic Blend Films: An in Situ Viewpoint. *Chem. Rev.* **2017**, *117*, 6332−6366.
(36) Inal, S.; Malliaras, G. G.; Rivnay, J. Benchmarking Organic Mixed Conductors for Transistors. *Nat. Commun.* **2017**, *8*, No. 1767.
(37) Flagg, L. Q.; Giridharagopal, R.; Guo, J.; Ginger, D. S. Anion-Dependent Doping and Charge Transport in Organic Electrochemical Transistors. *Chem. Mater.* **2018**, *30*, 5380−5389.
(38) Snowden, M. E.; Güell, A. G.; Lai, S. C. S.; McKelvey, K.; Ebejer, N.; O'Connell, M. A.; Colburn, A. W.; Unwin, P. R. Scanning Electrochemical Cell Microscopy: Theory and Experiment for Quantitative High Resolution Spatially-Resolved Voltammetry and Simultaneous Ion-Conductance Measurements. *Anal. Chem.* **2012**, *84*, 2483−2491.
(39) Stafford, C. M.; Roskov, K. E.; Epps, T. H.; Fasolka, M. J. Generating Thickness Gradients of Thin Polymer Films via Flow Coating. *Rev. Sci. Instrum.* **2006**, *77*, No. 023908.
(40) Kayunkid, N.; Uttiya, S.; Brinkmann, M. Structural Model of Regioregular Poly(3-Hexylthiophene) Obtained by Electron Diffraction Analysis. *Macromolecules* **2010**, *43*, 4961−4967.
(41) Lim, E.; Glaudell, A. M.; Miller, R.; Chabinyc, M. L. The Role of Ordering on the Thermoelectric Properties of Blends of Regioregular and Regiorandom Poly(3-hexylthiophene). *Adv. Electron. Mater.* **2019**, *5*, No. 1800915.
(42) Schroeder, P. von. Über Erstarrungs- Und Quellugserscheinungen von Gelatine. *Z. Phys. Chemie* **1903**, *45U*, 75−117.
(43) Weber, A. Z.; Newman, J. Transport in Polymer-Electrolyte Membranes. *J. Electrochem. Soc.* **2004**, *151*, A311.
(44) Thelen, J. L.; Wu, S.-L.; Javier, A. E.; Srinivasan, V.; Balsara, N. P.; Patel, S. N. Relationship between Mobility and Lattice Strain in Electrochemically Doped Poly(3-Hexylthiophene). *ACS Macro Lett.* **2015**, *4*, 1386−1391.
(45) Guardado, J. O.; Salleo, A. Structural Effects of Gating Poly(3-hexylthiophene) through an Ionic Liquid. *Adv. Funct. Mater.* **2017**, *27*, No. 1701791.
(46) Wang, S.; Ha, M.; Manno, M.; Daniel Frisbie, C.; Leighton, C. Hopping Transport and the Hall Effect near the Insulator−Metal Transition in Electrochemically Gated Poly(3-Hexylthiophene) Transistors. *Nat. Commun.* **2012**, *3*, No. 1210.
(47) Bittle, E. G.; Ro, H. W.; Snyder, C. R.; Engmann, S.; Kline, R. J.; Zhang, X.; Jurchescu, O. D.; DeLongchamp, D. M.; Gundlach, D. J. Dependence of Electrical Performance on Structural Organization in Polymer Field Effect Transistors. *J. Polym. Sci., Part B: Polym. Phys.* **2017**, *55*, 1063−1074.
(48) Lim, E.; Peterson, K. A.; Su, G. M.; Chabinyc, M. L. Thermoelectric Properties of Poly(3-Hexylthiophene) (P3HT) Doped with 2,3,5,6-Tetrafluoro-7,7,8,8-Tetracyanoquinodimethane (F 4 TCNQ) by Vapor-Phase Infiltration. *Chem. Mater.* **2018**, *30*, 998−1010.

https://doi.org/10.1021/acsami.2c06169
ACS Appl. Mater. Interfaces 2022, 14, 29052−29060